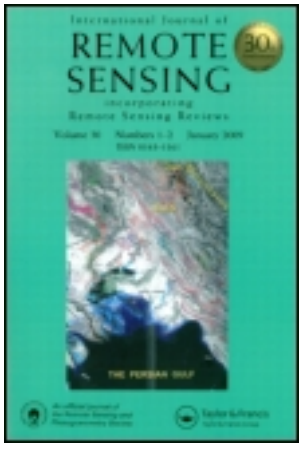

International Journal of Remote Sensing

Publication details, including instructions for authors and subscription information:
http://www.tandfonline.com/loi/tres20

Ocean remotely sensed image analysis using two-dimensional continuous wavelet transforms

Li-Chung Wu [a], Laurence Zsu-Hsin Chuang [b], Dong-Jiing Doong [c] & Chia Chuen Kao [a]

[a] Department of Hydraulic and Ocean Engineering, National Cheng Kung University, Tainan, Taiwan

[b] Institute of Ocean Technology and Marine Affairs, National Cheng Kung University, Tainan, Taiwan

[c] Department of Marine Environmental Informatics, National Taiwan Ocean University, Keelung, Taiwan

Available online: 09 Aug 2011

To cite this article: Li-Chung Wu, Laurence Zsu-Hsin Chuang, Dong-Jiing Doong & Chia Chuen Kao (2011): Ocean remotely sensed image analysis using two-dimensional continuous wavelet transforms, International Journal of Remote Sensing, 32:23, 8779-8798

To link to this article: http://dx.doi.org/10.1080/01431161.2010.534511

International Journal of Remote Sensing
Vol. 32, No. 23, 10 December 2011, 8779–8798

Taylor & Francis
Taylor & Francis Group

Ocean remotely sensed image analysis using two-dimensional continuous wavelet transforms

LI-CHUNG WU†, LAURENCE ZSU-HSIN CHUANG*‡, DONG-JIING DOONG§ and CHIA CHUEN KAO†

†Department of Hydraulic and Ocean Engineering, National Cheng Kung University, Tainan, Taiwan

‡Institute of Ocean Technology and Marine Affairs, National Cheng Kung University, Tainan, Taiwan

§Department of Marine Environmental Informatics, National Taiwan Ocean University, Keelung, Taiwan

(*Received 24 August 2009; in final form 27 September 2010*)

Ocean remote sensing is a useful way to obtain ocean wave information. Due to possible inhomogeneities from remotely sensed images, the current work proposes issues concerning ocean wave image analysis using the two-dimensional continuous wavelet transforms (2-D CWTs) to calculate local wave image spectra from inhomogeneous images. To optimize the algorithm of the 2-D CWT for wave image analysis, this work explores ideal parameter values for the wavelet function. The current study also analyses the limits of spatial image resolution and wave image size. After implementing the 2-D CWT on satellite and X-band radar images, this study presents local image spectra and ocean wave information from all the ocean images. These local image spectra reveal the phenomenon of wave refraction and wave nonlinearity nearshore. Compared to real wave spectra, the wavelet spectra present accurate results to describe local wave features in the spatial frequency domain.

1. Introduction

The ocean possesses ever-increasing global significance to human life, which makes increasing oceanic activities unavoidable. Ocean waves are one of the most significant phenomena in ocean environments and have attracted attention and comment throughout recorded history. Wave information is the basis for performance improvements of ocean and coastal activities. Engineering, navigation, harbour construction, fishing and cultivation, coastal disaster protection, recreation and even defence capabilities have become much more dependent on the availability of long-term, stable and high-quality ocean wave information. Ocean monitoring plays an important role in describing wave characteristics and can be broadly classified into two categories: *in situ* measurement and remote sensing. Various *in situ* measurements have been developed and improved for better quality. Most *in situ* measurement techniques are designed for monitoring ocean wave information in the time domain, and it is not as easy to

*Corresponding author. Email: laurence.chuang@gmail.com

International Journal of Remote Sensing
ISSN 0143-1161 print/ISSN 1366-5901 online © 2011 Taylor & Francis
http://www.tandf.co.uk/journals
http://dx.doi.org/10.1080/01431161.2010.534511

collect wave information in the space domain from the present *in situ* measurement instruments. An ocean wave field obtained by remote-sensing techniques is a useful way to present wave features in space domain. By the mid 1960s, researchers identified the basic processes responsible for the evolution of the ocean wave spectrum (Young 1999), and spectrum analysis has also become one of the main issues in studying ocean waves using remote-sensing technologies (Alpers and Hasselmann 1978, Young *et al.* 1985). A spectrum is the key to obtaining wave information such as wave number, wave direction and wave energy. Analysis algorithms are necessary to extract the spectrum from the image. The algorithm of a two-dimensional Fourier transform (2-D FT) has often been applied in the past to calculate the image spectrum (Gangeskar 2002, Nieto Borge *et al.* 2004), and is one of the most commonly used methods for identifying periodic components in stationary data.

To analyse the image using 2-D FT theory, spatial homogeneity within the observed area is assumed. The definition of spatial homogeneity is similar to temporal stationarity. Priestley (1991) statistically defined it as: A series $\mathbf{X}_t$ is called 'stationary' if, loosely speaking, its statistical properties do not change with time. More precisely, $\mathbf{X}_t$ is completely stationary if, for any set of times $t_1, t_2, \ldots, t_n$ and any integer z, the joint probability distribution of $\{X_{t_1}, X_{t_2}, \ldots, X_{t_n}\}$ is identical to the joint probability distribution of $\{X_{t_1+z}, X_{t_2+z}, \ldots, X_{t_n+z}\}$ (Kinsman 1965, Priestley 1991). Similarly, 'homogeneity' implies that the statistical properties do not change with space. It is recognized that most geophysical quantities are typically non-stationary and inhomogeneous in the time and space domains. While the evidence from geophysical quantities for abrupt changes is quite clear, the mechanisms driving these changes is less clear, and they are still the subject of active research (Cracknell and Varotsos 2007). These non-stationarities and inhomogeneities often conceal existing correlations into examined spatio-temporal series. Therefore, instead of applying conventional analyses, researches should use new analytical techniques capable of eliminating non-stationarities in the data (Varotsos *et al.* 2007).

The signals from ocean waves also show non-stationarities and inhomogeneities. Tayfun (1984) indicated that as ocean waves propagate from a homogeneous region, such as deep water, into a region with uneven underwater topography, their characteristics vary spatially. In a shallow bay or estuary, ocean waves may become shallow water waves during their development process. Waves propagating in a shallow water region gradually change in wavelength and direction due to the phenomenon of wave refraction. To analyse the inhomogeneous wave field image, Chen and Chen (1994) applied window Fourier transform (WFT) theory. The solution is to divide the image into small windows so that the wave field image is assumed to be homogeneous inside the window range in which the FT can be applied. However, the proper window size is often unknown. A wide window collects enough wave information from the wave field image, but wave features may still be inhomogeneous within the window. A narrow window prevents wave inhomogeneity, but wave information from the small image may not be enough to calculate the spectrum.

Wavelet transforms (WTs) and detrended fluctuation analysis (DFA) are currently among the most frequently used tools for non-stationary and inhomogeneous data analysis. Some recent studies have applied WT and DFA to the non-stationary time series of different geophysical quantities (Gorman and Hicks 2005, Varotsos and Kirk-Davidoff 2006, Varotsos *et al.* 2006, 2007, Lee *et al.* 2007). In addition to one-dimensional time series analysis, the high-dimensional WT algorithm for image analysis is also complete (Carlson 1995). Image spectrum analysis from wave images

by the 2-D CWT should also be practicable, but this issue has received little attention. To extract accurate spectra from an inhomogeneous wave field image, the 2-D CWT algorithm should be applicable. The present article extracts the spectra by 2-D CWT from the ocean remotely sensed image to reveal inhomogeneous ocean wave phenomena. This work explores appropriate parameter values from the wavelet function and image format to optimize the 2-D CWT algorithm on image analysis. This study applies satellite images and X-band radar to discuss the ocean wave phenomena.

2. Theoretical preliminaries

2.1 *The 2-D CWT algorithm*

The CWT is often compared to the FT, in which signals are represented as a sum of sine waves or cosine waves. The CWT breaks the signal into different kinds of wavelets, which then can be scaled, shifted and rotated (figure 1). In the study of Antoine *et al.* (2004), a complete theory of 2-D CWT was proposed and the application of image analysis was discussed. The 2-D CWT of the image function $s(\boldsymbol{x}) = s(x, y)$ for a transformed wavelet function $\psi_{\boldsymbol{b},\theta,a}(\boldsymbol{x})$ is given by:

$$W(\boldsymbol{b}, \theta, a) = C_{\psi}^{-0.5} a^{-1} \int_{\mathrm{R}^2} \psi^* \left[a^{-1} \mathbf{r}_{-\theta} (\boldsymbol{x} - \boldsymbol{b}) \right] s(\boldsymbol{x}) \, \mathrm{d}^2 \boldsymbol{x}, \tag{1}$$

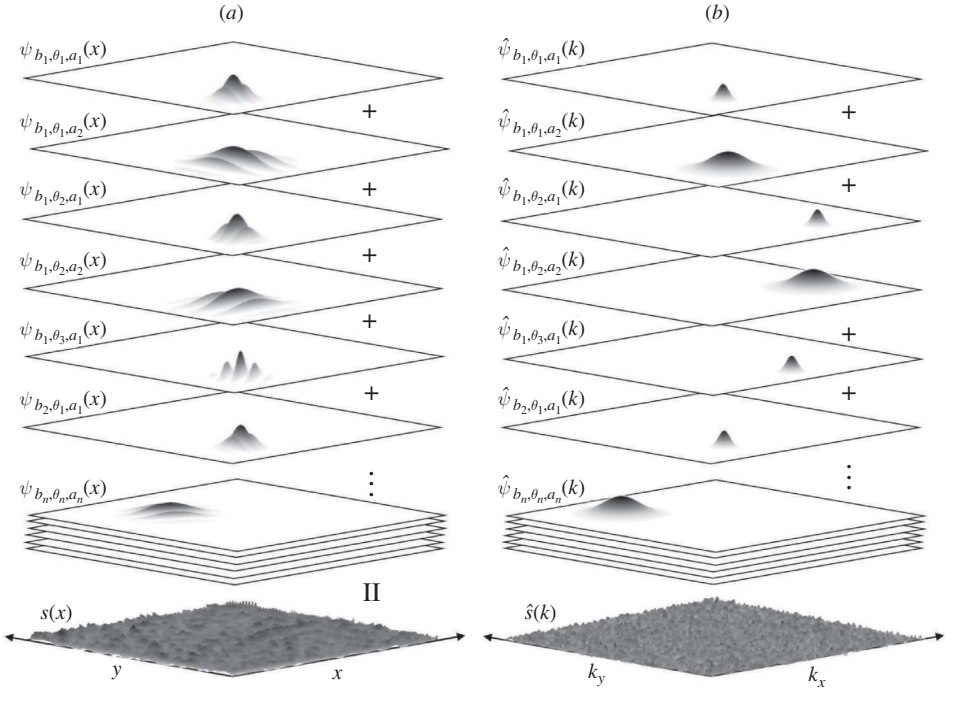

Figure 1. Schematic illustration of a wave image broken into various wavelets in (*a*) the space domain and (*b*) spatial frequency domain.

$$C_\psi = (2\pi)^2 \int_{R^2} \left[\left| \hat{\psi}(\boldsymbol{k}) \right|^2 \Big/ |\boldsymbol{k}|^2 \right] d^2\boldsymbol{k} < \infty, \tag{2}$$

in which ψ^* is the complex conjugate of the wavelet function ψ and function $\hat{\psi}$ is the mother wavelet function ψ in Fourier space. R^2 is a complex-valued function defined on the real plane as square integrable. $\boldsymbol{k} = (k_x, k_y)$ is the spatial frequency and is called the wavenumber in the field of coastal engineering and marine science. The scaling parameter a, a non-dimensional scale factor, is related to the dilated spatial frequency. The factor a^{-1} is a normalization that gives all dilated versions of the mother wavelet the same energy, that is it is the ratio of the size of the dilated wavelet to the size of the mother wavelet. The translation parameter $\boldsymbol{b} = (b_x, b_y)$ corresponds to the position of the wavelet as it shifts through the space domain. The rotation matrix $\mathbf{r}_{-\theta}$ with a rotation angle θ, which rotates the wavelet in spatial coordinates, is usually defined as:

$$\mathbf{r}_{-\theta} = \begin{pmatrix} \cos\theta & \sin\theta \\ -\sin\theta & \cos\theta \end{pmatrix}, \quad 0 \le \theta < 2\pi. \tag{3}$$

To implement equation (1), it is necessary to first choose a proper mother wavelet function ψ. The Morlet wavelet function, which is a directionally selective and complex-valued wavelet function, is chosen here for detecting the directional wave information from the wave image. The Morlet wavelet function is the result of sine/cosine functions multiplying a decayed function in which exponential functions are used. In other words, the Morlet wavelet function can be seen as a kind of decayed sine/cosine function in the space domain:

$$\psi(\boldsymbol{x}) = \exp\left(-0.5\,|\mathbf{A}\boldsymbol{x}|^2\right) \exp\left(i\boldsymbol{k}_0\boldsymbol{x}\right) - \exp\left(-0.5\,|\mathbf{A}\boldsymbol{x}|^2\right) \exp\left(-0.5\left|\mathbf{A}^{-1}\boldsymbol{k}_0\right|^2\right). \tag{4}$$

The vector $\boldsymbol{k}_0$ controls the oscillation of wavelet function. $\mathbf{A} = \mathrm{diag}[\varepsilon^{-0.5}, 1]$, $\varepsilon \ge 1$, is an anisotropy matrix. The parameter ε controls the wavelet function window in the space and spatial frequency domains. We will discuss the effects of $\boldsymbol{k}_0$ and ε upon wave image analysis in later sections. For the theory of a spectrum, sine/cosine functions are always the components used in analysis. To obtain accurate local spectrum, the Morlet wavelet function should be applicable for image analysis. For computational application, the continuous function of the 2-D CWT shown in equation (1) should be described discretely:

$$W\left(b_{x_k}, b_{y_l}, \theta_m, a_n\right) = C_\psi^{-0.5} a_n^{-1} \sum_{p=1}^{N_x} \sum_{q=1}^{N_y} \psi^*\left[a_n^{-1}\mathbf{r}_{-\theta m}\left(x_p - b_{x_k}, y_q - b_{y_l}\right)\right] s\left(x_p, y_q\right) \Delta x_p \Delta y_q, \tag{5}$$

in which N_x and N_y are the total sampling numbers in the x and y directions of the wave field. Let N_{b_x}, N_{b_y}, N_θ and N_a be the operation counts of the parameters b_{x_k}, b_{y_l}, θ_m and a_n in the calculation. b_{x_k}, b_{y_l}, θ_m and a_n denote discrete variables of b_x, b_y, θ and a. The subscripts k, l, m and n denote the discrete symbols. To calculate $W(b_{x_k}, b_{y_l}, \theta_m, a_n)$ from every location (x_p, y_q) of the wave field image, $N_x = N_{b_x}$ and $N_y = N_{b_y}$ should be satisfied. Therefore, the total operation counts by equation (5)

should be $N_x^2 N_y^2 N_a N_\theta$ in the image analysis. It is possible to reduce the operation counts by the WT in the Fourier space:

$$W\left(b_{x_k}, b_{y_l}, \theta_m, a_n\right) = C_\psi^{-0.5} a_n \sum_{p=1}^{N_{k_x}} \sum_{q=1}^{N_{k_y}} \mathrm{e}^{\mathrm{i}\left(b_{x_k} k_{x_p} + b_{y_l} k_{y_q}\right)} \hat{\psi}^* \left[a_n \mathbf{r}_{-\theta m}\left(k_{x_p}, k_{y_q}\right)\right] \hat{s}\left(k_{x_p}, k_{y_q}\right) \Delta k_{x_p} \Delta k_{y_q}, \tag{6}$$

$$\hat{\psi}(\boldsymbol{k}) = \varepsilon^{0.5} \left\lfloor \exp\left(-0.5 \left|\mathbf{A}^{-1}\left(\boldsymbol{k} - \boldsymbol{k}_0\right)\right|^2\right) - \exp\left(-0.5 \left|\mathbf{A}^{-1}\boldsymbol{k}_0\right|^2\right) \exp\left(-0.5 \left|\mathbf{A}^{-1}\boldsymbol{k}\right|^2\right) \right\rfloor. \tag{7}$$

Function $\hat{\psi}$ is the mother wavelet function ψ in Fourier space. $\hat{\psi}^*$ is the complex conjugate of the function $\hat{\psi}$. N_{k_x} and N_{k_y} are the operation counts of k_{x_p} and k_{y_q}. Based on the theory of discrete image signal analysis, N_{k_x} and N_{k_y} should equal N_x and N_y. Equation (5) can be simplified using the Inverse Fast Fourier transform (IFFT) algorithm:

$$W\left(b_{x_k}, b_{y_l}, \theta_m, a_n\right) = C_\psi^{-0.5} a_n T\left\{\hat{\psi}^*\left[a_n \mathbf{r}_{-\theta m}\left(k_{x_p}, k_{y_q}\right)\right] \hat{s}\left(k_{x_p}, k_{y_q}\right)\right\}, \tag{8}$$

in which T{} denotes the algorithm of the IFFT. Using the numerical technique of IFFT, the total operation counts obtained using equation (8) should be reduced to $N_x \log_2(N_x) \times N_y \log_2\left(N_y\right) \times N_a \times N_\theta$. Compared with equation (5), equation (8) does reduce the total operation counts. Equation (8) shows that the result analysed by 2-D CWT is a function of scaling, translation and rotation parameters. To obtain the ocean wave information from equation (8), the current work transforms the function $W\left(b_{x_k}, b_{y_l}, \theta_m, a_n\right)$ into the image spectrum. As shown in equation (8), $\hat{\psi}_{\boldsymbol{b},\theta,a}(\boldsymbol{k})$ is the wavelet function. The relationship between the wavelet function $\hat{\psi}_{\boldsymbol{b},\theta,a}(\boldsymbol{k})$ and the mother wavelet function $\hat{\psi}(\boldsymbol{k})$ is defined as:

$$\hat{\psi}_{\boldsymbol{b},\theta,a}(\boldsymbol{k}) = a \exp\left(-\mathrm{i}\boldsymbol{b}\boldsymbol{k}\right) \hat{\psi}\left[a\mathbf{r}_{-\theta}(\boldsymbol{k})\right]. \tag{9}$$

The influence of scaling, translation and rotation parameters upon the wavelet function in the spatial frequency domain is shown in figure 2. Equation (9) shows that the spatial frequency (wavenumber) could be transformed from $\boldsymbol{k}$ into $a\mathbf{r}_{-\theta}(\boldsymbol{k})$ after scaling, shifting and rotating a mother wavelet function. As shown in equation (7), $\boldsymbol{k}_0$ is the peak location of the mother Morlet function in Fourier space. After transforming, a new location of the peak energy of the Morlet wavelet function in Fourier space becomes $\boldsymbol{k}_\mathrm{n}$. The relationship between $\boldsymbol{k}_0$ and $\boldsymbol{k}_\mathrm{n}$ is given as:

$$\boldsymbol{k}_\mathrm{n} = \boldsymbol{k}_0 \big/ (a\mathbf{r}_{-\theta}). \tag{10}$$

Equation (10) reveals that we can obtain the spatial frequency $\boldsymbol{k}_\mathrm{n}$ from parameters a and θ. The shifting parameter $\boldsymbol{b}$ of the 2-D CWT stands for the shifting distance of the wavelet function from the original location of the wave image. In other words, it presents the calculated location $\boldsymbol{x}$ of the wavelet function from the image directly. Hence, the function $W\left(b_{x_k}, b_{y_l}, \theta_m, a_n\right)$ could be expressed as $W(\boldsymbol{x}, \boldsymbol{k}_\mathrm{n})$, which represents the local spectrum $W(\boldsymbol{k}_\mathrm{n})$ from different spatial locations $\boldsymbol{x}$.

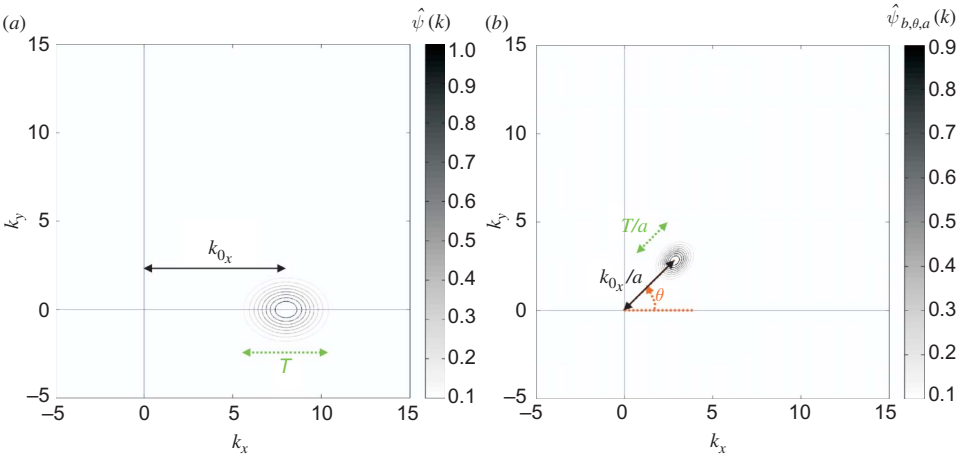

Figure 2. Relationship between (*a*) mother wavelet function and (*b*) wavelet function in the spatial frequency domain.

2.2 *Simplification of the wavelet function in Fourier space*

Figure 3 shows that the Morlet wavelet functions are decay functions in the space domain and in the spatial frequency domain (Fourier space). In other words, $\psi(\boldsymbol{x})$ and $\hat{\psi}(\boldsymbol{k})$ tend to zero if the values of $\boldsymbol{x}$ and $\boldsymbol{k}$ increase. This means $\psi(\boldsymbol{x})$ and $\hat{\psi}(\boldsymbol{k})$ are approximately zero if the values of $\boldsymbol{x}$ and $\boldsymbol{k}$ are large enough. The zero parts of the wavelet function cannot affect the convolution in equation (1). Only the non-zero parts of the wavelet function need to be calculated in the wavelet analysis, so the calculated amounts can be reduced by omitting the calculations from the zero parts of

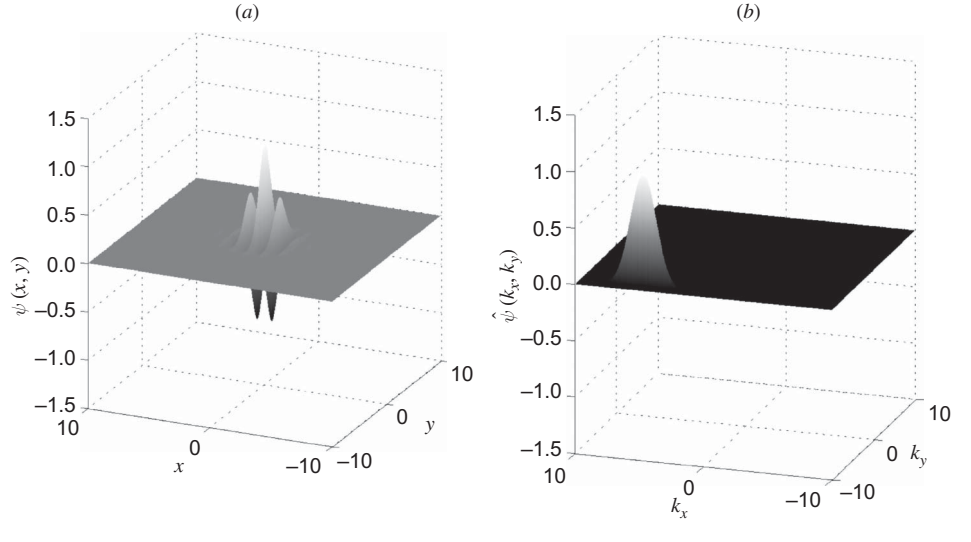

Figure 3. Morlet wavelet function in (*a*) the space domain and (*b*) its spatial frequency domain.

the wavelet function. The calculations can be quickened by simplifying the wavelet function. Equation (7) shows that the function $\hat{\psi}(\boldsymbol{k}) = \hat{\psi}(k_x, k_y)$ should be symmetrical in the x and y directions if the matrix $\mathbf{A} = \mathrm{diag}[1, 1]$. In other words, the decay of $\hat{\psi}(k_x, k_y)$ in the x and y directions should be the same. To explain the process more simply, the function $\hat{\psi}(k_x, k_y)$ is simplified as $\hat{\psi}(k_x)$ here. The function $\hat{\psi}(k_x)$ is zero if k_x is large enough. To determine the non-zero range of the mother wavelet function in the spatial frequency domain, the standard deviation (σ_{k_x}) of the mother wavelet function is used here:

$$\sigma_{k_x} = \left[\int_{-\infty}^{\infty} (k_x - k_{c_x})^2 \left| \hat{\psi}(k_x) \right|^2 \mathrm{d}k_x \right]^{0.5}, \tag{11}$$

$$k_{c_x} = \left[\int_{-\infty}^{\infty} k_x \left| \hat{\psi}(k_x) \right|^2 \mathrm{d}k_x \right] \Big/ \left[\int_{-\infty}^{\infty} \left| \hat{\psi}(k_x) \right|^2 \mathrm{d}k_x \right], \tag{12}$$

in which k_{c_x} represents the centre of the mother wavelet function in the spatial frequency domain. Figure 4 shows the decay of the Morlet mother wavelet function. Based on equation (7), $\hat{\psi}(k_{c_x})$ should approximate to the maximum value of the mother wavelet function $\hat{\psi}_m$ in the whole Fourier space. Let $2D_s$ be the width of non-zero parts of the mother wavelet function. As figure 4 shows, $\hat{\psi}(k_x)$ is less than 1% of $\hat{\psi}_m$ if D_s is larger than $3.5\sigma_{k_x}$. This means $\hat{\psi}(k_x)$ is small enough and the convolution between the function $\hat{\psi}^*(k_x)$ and the image function $\hat{s}(k_x)$ cannot influence the result of the WT obviously if D_s is larger than $3.5\sigma_{k_x}$. For the purpose of simplifying the mother wavelet function, the current study suggests that the width of non-zero parts of $\hat{\psi}(k_x)$ be set up as the value over $7\sigma_{k_x}$.

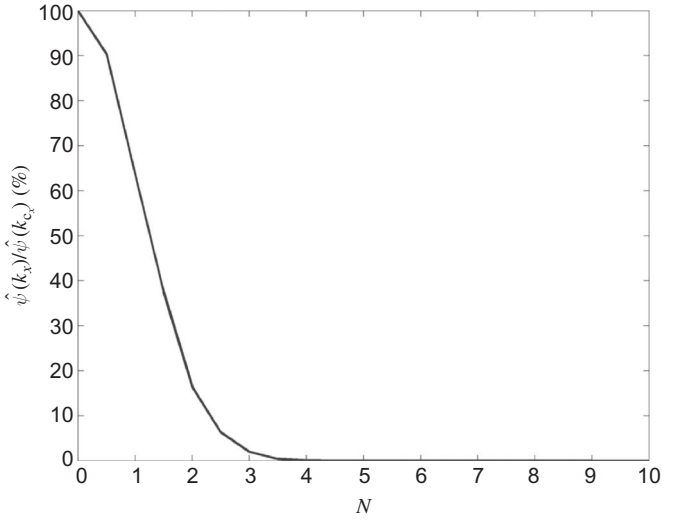

Figure 4. Decay of the Morlet mother wavelet function in the spatial frequency domain (D_s). $D_s = N_{\sigma_{kx}}$.

3. Optimization of the 2-D CWT algorithm for wave image analysis

To implement the algorithm for oceanic image analysis, some parameters of wavelet function and image conditions need to be determined. Here, we propose the proper values of these parameters to optimize this algorithm for image analysis.

3.1 *Influence of parameter k_0 upon the wavelet function*

Equation (4) showed the vector $\boldsymbol{k}_0 = (k_{0_x}, k_{0_y})$, which was not determined in the previous sections. if k_{0_x} and k_{0_y} are both non-zero, the direction of the wavelet function in space and spatial frequency domains (Fourier space) would be influenced by the values of k_{0_x} and k_{0_y}. Since the matrix $\mathbf{r}_{-\theta}$ from equation (1) was applied to control the direction of wavelet function, k_{0_y} was set to zero in this study. Figure 5 shows that k_{0_x} controls the peak spatial frequency in the spatial frequency domain. The peak location of the mother wavelet function in the spatial frequency domain equals k_{0_x}. The peak location of the mother wavelet function would be too close to the edge ($k_x = 0$) in the k_x domain if the value of k_{0_x} is too low. The wavelet function would be incomplete in these cases and influence the convolution result in equation (1). Therefore, it is necessary to determine whether k_{0_x} is large enough.

As shown in equation (13), let E_t be the total energy of the complete Morlet mother wavelet function, $E_\mathrm{r}(k_{0_x})$ is the total energy of the Morlet mother wavelet function with different k_{0_x}. Let R_n be the ratio between $E_\mathrm{r}(k_{0_x})$ and E_t. As shown in figure 6, R_n is larger than 99.9% if k_{0_x} is larger than 4. This means that the mother wavelet function is nearly complete if k_{0_x} is larger than 4. Antoine *et al.* (2004) pointed out that the second terms of equations (4) and (7) can be numerically negligible for $|\boldsymbol{k}_0| \geq 5.6$. To simplify the mother wavelet function, we adopt $\boldsymbol{k}_0 = (6, 0)$ to analyse the images in our study:

$$R_\mathrm{n}(k_{0_x}) = \left[E_\mathrm{r}(k_{0_x})/E_\mathrm{t}\right] \times 100\% = \left[\int_0^\infty \hat{\psi}(k_x, k_{0_x})\,\mathrm{d}k_x \Big/ E_\mathrm{t}\right] \times 100\%. \tag{13}$$

3.2 *Influence of the parameter ε on the wavelet function*

In addition to parameter $\boldsymbol{k}_0$, the parameter ε from the matrix $\mathbf{A}$ in equations (4) and (7) also influences wave image analysis by the 2-D CWT. Figure 7 shows that parameter ε also controls the non-zero size (the wavelet function window) in the

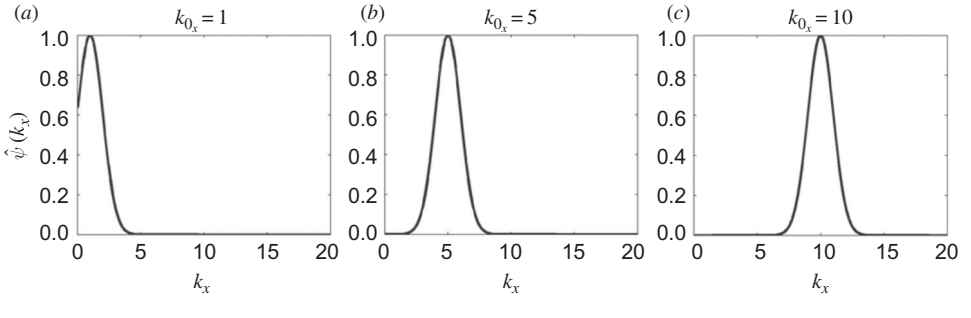

Figure 5. Influence of the parameter k_{0_x} upon the wavelet function in the spatial frequency domain.

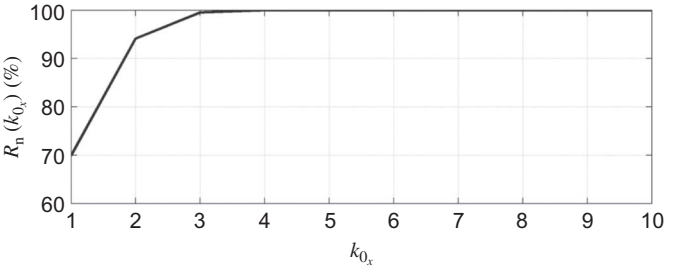

Figure 6. Influence of the parameter k_{0x} upon $R_n(k_{0x})$.

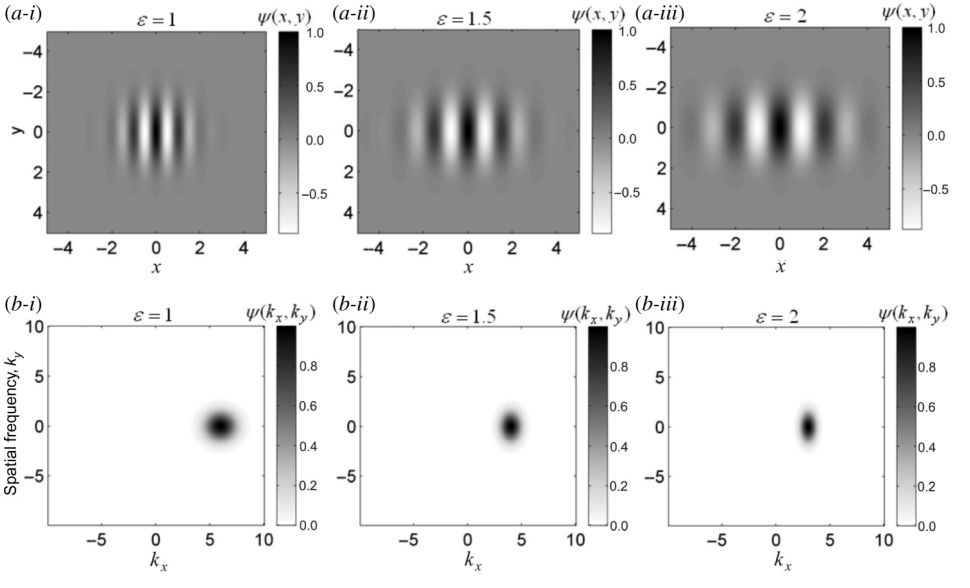

Figure 7. Relationship between the parameter ε and the non-zero size of the wavelet function in the space and spatial frequency domains.

space and spatial frequency domains. If the non-zero size is too large, the corresponding resolution would be poorer. According to the Heisenberg Uncertainty Principle (Van Name 1960), the resolutions between the space domain and spatial frequency domain are opposite. If the value of parameter ε increases, the resolution in the space domain would be poor, but the resolution in the spatial frequency domain would be precise. To verify the non-zero size of the wavelet function, the parameters σ_{k_x} and σ_x are described in equations (11) and (14):

$$\sigma_x = \left\{ \int_{-\infty}^{\infty} \left[x - \left(\int_{-\infty}^{\infty} x \left|\psi(x)\right|^2 \mathrm{d}x \Big/ \int_{-\infty}^{\infty} \left|\psi(x)\right|^2 \mathrm{d}x \right) \right]^2 \left|\psi(x)\right|^2 \mathrm{d}x \right\}^{0.5}, \qquad (14)$$

where σ_x and σ_{k_x} are the standard deviations of $\psi(x)$ and $\hat{\psi}(k_x)$, respectively. They are related to the non-zero areas of the mother wavelet function in the space domain and spatial frequency domain. Figure 8 shows that parameter σ_x increases if ε decreases.

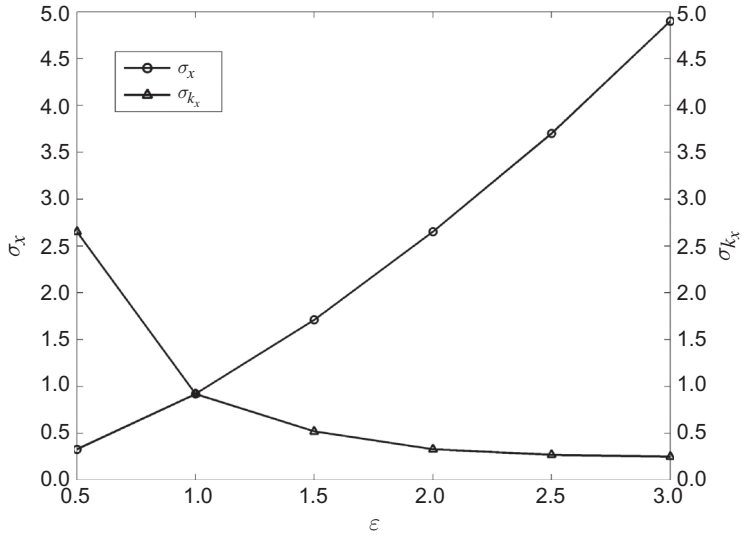

Figure 8. Relationship of the parameters ε, σ_{k_x} and σ_x.

On the contrary, parameter σ_{k_x} increases if ε increases. The resolution in the space domain and the spatial frequency domain are both important for wave image analysis. Therefore, parameters σ_x and σ_{k_x} should be as low as possible to obtain the ideal resolution of the wavelet function in both the space and spatial frequency domains. However, the Heisenberg Uncertainty Principle proves it is impossible to obtain the lowest values of σ_x and σ_{k_x} using the same ε. To obtain the balance between σ_x and σ_{k_x}, this work suggested that ε be set up with a value of 1.

3.3 *Ideal resolution of wave field image*

Wave image conditions are key to obtaining an accurate spectrum. Wave features for poorer spatial resolution of the wave image may be severely aliased (Jahne 1995). Significant wave information, such as wavenumber and wave direction, are influenced by poor wave image resolution. Based on the Nyquist sampling limit (Henderson and Lewis 1998), the case of wavelength longer than $2\Delta x$ can be analysed if the spatial resolution of the wave field is Δx for wave image analysis using the 2-D FT. In other words, the highest value in the spatial frequency domain is limited under $2\pi/(2\Delta x)$ if the spatial resolution of the wave field is Δx. However, $2\pi/(2\Delta x)$ may not be the spatial frequency limitation using the 2-D CWT. Figure 9 shows that part of the wavelet function would be cut off if the peak frequency of the wavelet function is close to the limitation $2\pi/(2\Delta x)$. This means an incomplete wavelet function would be used for cases of high-frequency wave analysis. Due to the influence of window width, it is necessary to use higher resolution in the 2-D CWT than in the 2-D FT. Here, we invest the reasonable limitation of the spatial frequency for image analysis using the 2-D CWT. As mentioned in the previous section, we first simplify the two-dimensional wavelet function to one dimension. Let $D_k\,(k_x)$ be the distance between k_{0_x} and k_x within the wavelet function:

$$D_k(k_x) = \left|k_x - k_{0_x}\right|, \tag{15}$$

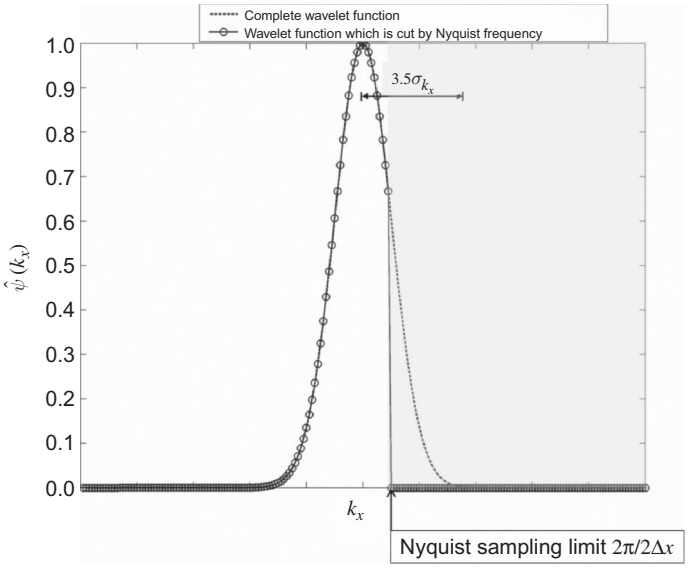

Figure 9. Influence of the Nyquist frequency limitation on the window width of the wavelet function. σ_x.

in which k_{0_x} was defined in the previous section. Let function P_k be the ratio between $\hat{\psi}(k_x)$ and $\hat{\psi}(k_{0_x})$:

$$P_k = \hat{\psi}(k_x) / \hat{\psi}(k_{0_x}). \tag{16}$$

The resolution condition of the image should depend upon wavelength. To determine the ideal resolution condition, the wavelength of ocean waves is used here. If the spatial frequency limitation does not cut off the wavelet function, P_k should match the theory curve in figure 10. This theory curve describes the decayed feature of wavelet function in the spatial frequency domain. Figure 10 reveals that the cases of wavelength under $3.5\Delta x$ are not long enough for wave image analysis using the 2-D CWT. The spatial frequency limitation using the 2-D CWT should be less than $2\pi/(3.5\Delta x)$. To obtain accurate results, the spatial resolution of wave image should be shorter than 1/3.5 the wavelength of the ocean wave conditions.

3.4 *Ideal size of the wave field image*

Due to the numerical technique of the IFFT used in equation (8), the size of the wave image in the space domain would influence the spectrum resolution in the spatial frequency domain. Here, we discuss the ideal size of the discrete wave image. As shown in equation (7), the second term can be omitted if $\boldsymbol{k}_0$ is large enough. Previous sections of this study suggest that the value of ε be set to 1 and k_{0_x} be set to 6. Hence, equation (7) can be simplified as:

$$\hat{\psi}(\boldsymbol{k}) = \exp\left(-0.5\,|\boldsymbol{k} - \boldsymbol{k}_0|^2\right). \tag{17}$$

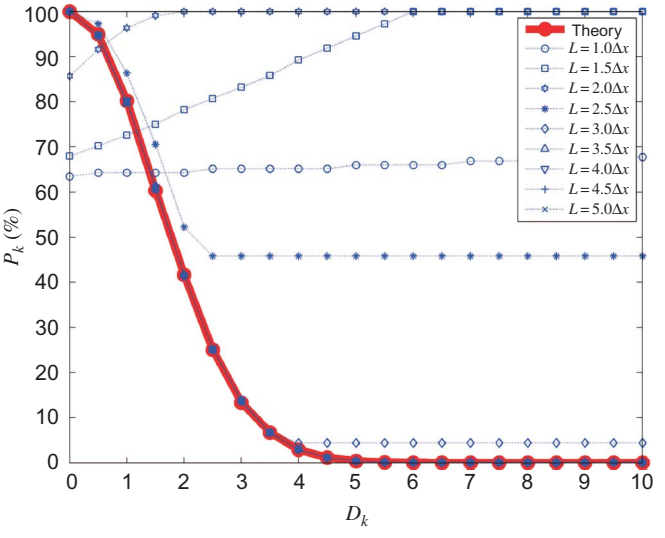

Figure 10. Relationship between D_k (k_x) and P_k.

For combining the relationship in equations (9) and (17), we obtain:

$$\hat{\psi}_{\boldsymbol{b},\theta,a}(\boldsymbol{k}) = a\exp\left(-\mathrm{i}\boldsymbol{b}\boldsymbol{k}\right)\exp\left[-0.5\left|a\mathbf{r}_{-\theta}\left(\boldsymbol{k}\right)-\boldsymbol{k}_0\right|^2\right]. \tag{18}$$

In the previous sections, we let the wavelet function oscillate only in the x direction, or $\boldsymbol{k}_0 = \left(k_{0_x},0\right)$. We can simplify the wavelet function as:

$$\hat{\psi}_{b_x,a}(k_x) = a\exp\left(-\mathrm{i}b_xk_x\right)\exp\left[-0.5\left|ak_x-k_{0_x}\right|^2\right]. \tag{19}$$

The term $\exp\left(-\mathrm{i}b_xk_x\right)$ from equation (19) satisfies:

$$\left|\exp\left(-\mathrm{i}b_xk_x\right)\right| = 1. \tag{20}$$

Therefore, equation (17) can be simplified as:

$$\left|\hat{\psi}_{b_x,a}\left(k_x\right)\right| = a\exp\left(-0.5\left|ak_x-k_{0_x}\right|^2\right). \tag{21}$$

Equation (19) presents the continuous function of the CWT. Consider the physical space series sampled with sampling space Δx. The total amount of dimensional space for N_x points, defined as the number of sample points of the wavelet, is $N_x\Delta x$. If the total non-dimensional space length is $2X$, it is mapped for N_x points (Jordan *et al.* 1997, Chuang *et al.* 2008). Figure 11 describes the relationship. The relationship between the dimensional and non-dimensional sampling spaces can be obtained through the number of sample points of the wavelet function:

$$\left|\hat{\psi}_{b_x,a}\left(k_x\right)\right| = a\exp\left\{-0.5\left|ak_x\left[\left(N_x\Delta x\right)/\left(2X\right)\right]-k_{0_x}\right|^2\right\}. \tag{22}$$

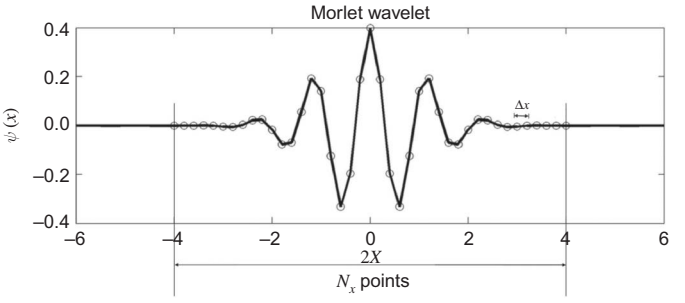

Figure 11. Relationships between measured spatial samples and wavelet function samples. N_x represents the measured fluctuation sample points and Δx is the sampling space.

As shown in equation (22), Let k_{x_p} represent the peak spatial frequency of $\left|\hat{\psi}_{b_x,a}\right|$, and the value of $\left|\hat{\psi}_{b_x,a}\left(k_{x_p}\right)\right|$ would be largest if:

$$k_{x_p} = \left(2Xk_{0_x}\right)/(aN_x\Delta x). \tag{23}$$

The value of $\left|\hat{\psi}_{b_x,a}\left(k_{x_p}\right)\right|$ would be equal to a if equation (23) is satisfied. To determine the size of wave field images, the non-zero part of $\left|\hat{\psi}_{b_x,a}\right|$ needs to be defined. Let k_{x_N} be the edge of the non-zero part of $\left|\hat{\psi}_{b_x,a}\right|$; this means that the value of $\left|\hat{\psi}_{b_x,a}\left(k_x\right)\right|$ can be seen to be zero if $k_x > k_{x_N}$. We define R_t as:

$$R_t < \left|\hat{\psi}_{b_x,a}\left(k_{x_N}\right)\right| \Big/ \left|\hat{\psi}_{b_x,a}\left(k_{x_p}\right)\right| = \exp\left\{-0.5\left[\left(\frac{ak_{x_N}\Delta xN_x}{2X}\right) - k_{0_x}\right]^2\right\}. \tag{24}$$

The proper size of the wave image can be obtained after determining the value of R_t:

$$N_x > \left[(2X)/\left(a\Delta xk_{x_N}\right)\right]\left\{k_{0_x} + \left[-2\ln\left(R_t\right)\right]^{0.5}\right\}. \tag{25}$$

4. Ocean remotely sensed image analysis

To examine the validity of the technique presented above and to test the algorithm for computing the 2-D CWT, Chuang *et al.* (2008) applied simulated wave images to verify the accuracies of image spectra using the 2-D CWT. Based on this study, the comparisons between estimations and theoretical values for wave parameters show that the 2-D CWT is capable of identifying the directional spectra and wave properties. Here, we use a satellite image and X-band radar image to verify the practicability of the 2-D CWT. Satellite based remote-sensing instruments can now provide a large-scale view of the wave field. The source for the satellite image dataset is the Global Land Cover Facility (www.landcover.org). Fine-resolution imagery from QuickBird is collected here. Figure 12 shows the wave field image near the Ujong Kulon National Park in Indonesia with a mean pixel resolution of 0.66 m. The frame in figure 12 is a

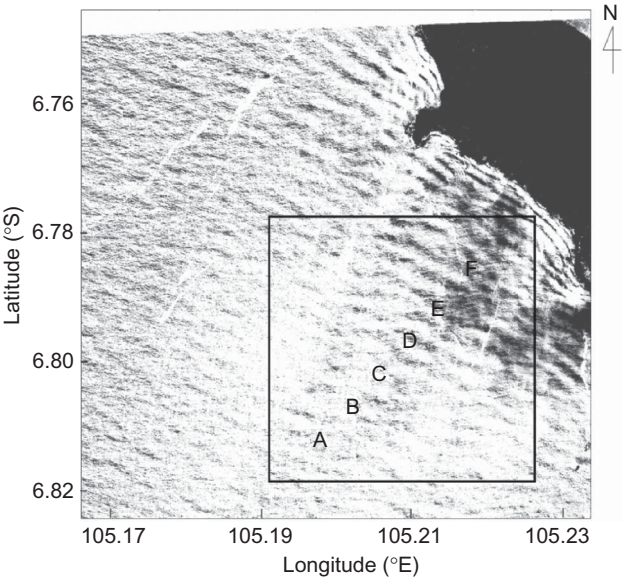

Figure 12. Satellite image near the Ujong Kulon National Park in Indonesia.

sub-image that we have extracted for image analysis. Figure 13 shows the image spectrum analysed by the 2-D FT. The spectrum corresponds to one wave component and its mirror one in the opposite direction. This means the wave directions are ambiguous for judging the 180° difference when a single wave image is transformed into the image spectrum. The ambiguity could be eliminated by adopting a series of wave images. In figure 13, k_x and k_y indicate the spatial frequency of the ocean waves in the x and y directions. Based on wave theory, the ocean wavelength L can be obtained from k:

$$L = 2\pi/k, \tag{26}$$

$$k = \left(k_x^2 + k_y^2\right)^{0.5}. \tag{27}$$

Wave direction α can also be obtained:

$$\alpha = \tan^{-1}\left(k_x/k_y\right). \tag{28}$$

The image spectrum using the FT describes these wave features in the spatial frequency domain. However, verifying local wave information of different areas from the whole image is difficult because many different ocean wave components exist within the whole ocean image. Compared to the spectra using the 2-D FT, figure 14 presents the image spectra from the same sub-image using the 2-D CWT. The sub-image size is 1024 × 1024 pixels. Based on the theories of 2-D CWT and discrete mathematics, we obtain 1024 × 1024 image spectra from the 1024 × 1024 pixels sub-image. To display the calculated results simply on hard copy paper, we only present six spectra from location A to location F, which are marked on figure 12. We observe that

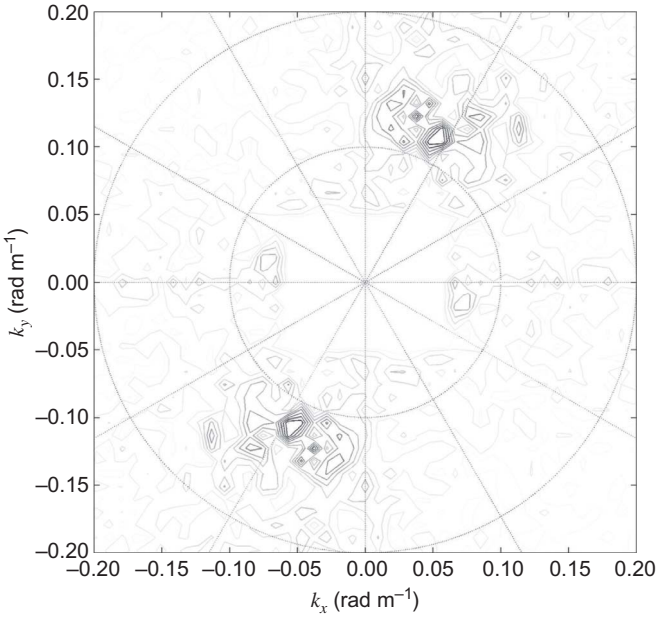

Figure 13. 2-D FT image spectrum analysed from the satellite image.

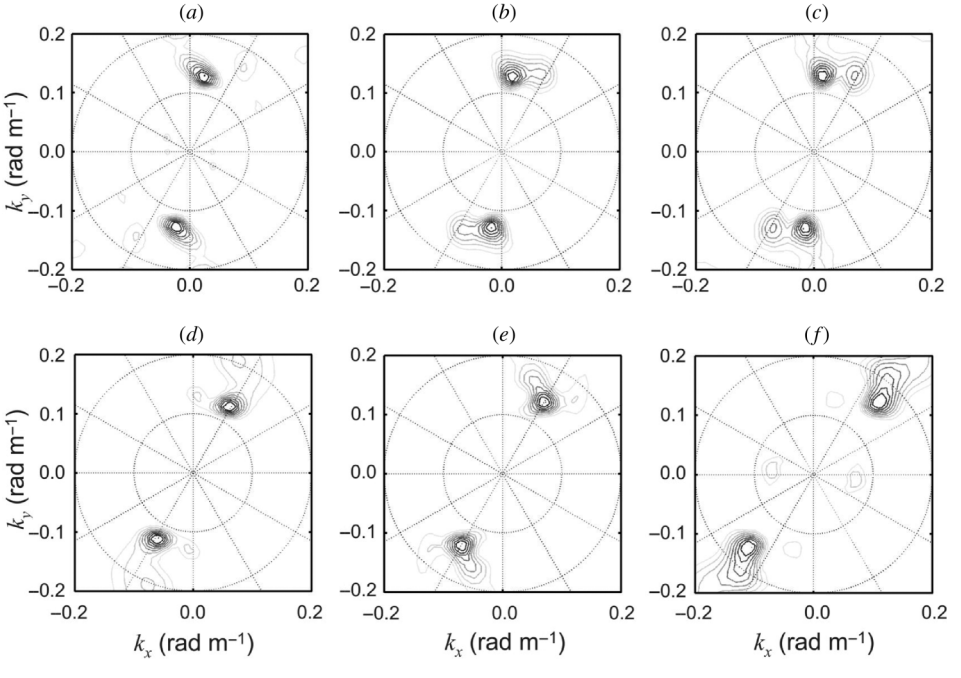

Figure 14. 2-D CWT image spectra analysed from the satellite image. Points A to F can be found in the image shown in figure 12.

peak wavenumber and dominant wave direction for each wave component gradually change at different locations of the image. This shows that the wavenumber corresponding to the energy contour at location A (offshore) gradually moves from a lower value to a higher one at location F (nearshore). Spectral energy at a higher wavenumber is more scattered than that at a lower wavenumber. This is because the higher wavenumber component has lower resolution in the spatial frequency domain and higher resolution in the space domain, known as the Heisenberg Uncertainty Principle (Van Name 1960). The spectra also present the dominant direction of the energy density as the spectrum moves from SSW to SW, revealing the wave refraction phenomenon in the coastal area. The energy distribution from the Fourier spectrum is similar to the energy distribution from the wavelet spectra. However, the wavelet spectra are capable of presenting local wave features from different areas of the satellite image.

This study also used images from X-band radar, which make it possible to obtain ocean wave information (Young *et al.* 1985). Figure 15 shows radar images in the southern part of Taiwan. The water depth in the area ranges from 5 to 100 m. The current work collects 30 radar images from this area. Figure 16 shows that an example using the 2-D CWT also displays a similar phenomenon to satellite image results. The 2-D CWT spectra present local ocean wave features from different radar image locations. This study has applied one-dimensional real wave spectra from an *in situ* data buoy to show detailed spectral features. To compare the real wave spectra and image spectra, the 2-D image spectra $W(k_x,k_y)$ were integrated into one-dimensional spectra $W(k)$ via equation (27). Figure 17 shows a comparison of the real wave spectrum and image spectra extracted by the FT and WT. The image spectra extracted by the FT and WT in this study are called Fourier spectra and wavelet spectra, respectively. The image spectra are calculated from the grey value on the remotely sensed images. Unlike

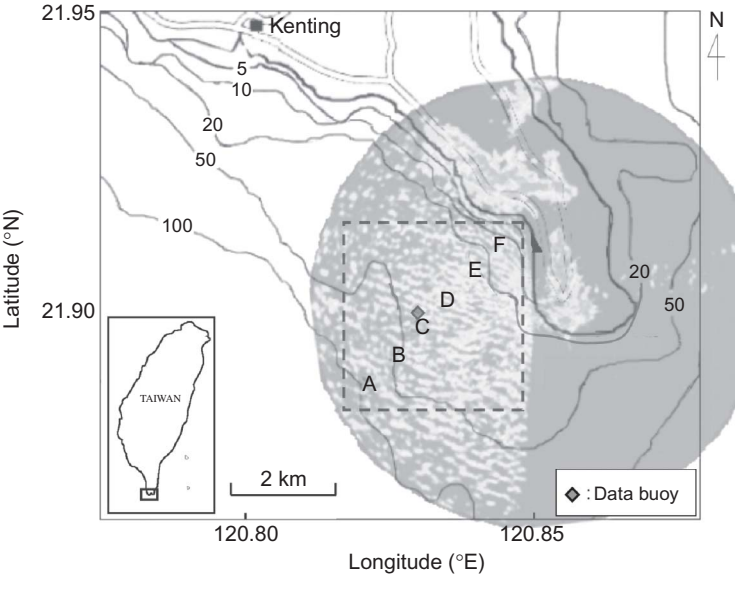

Figure 15. X-band radar image observed in the southern part of Taiwan. The grey circle is the area covered by the image.

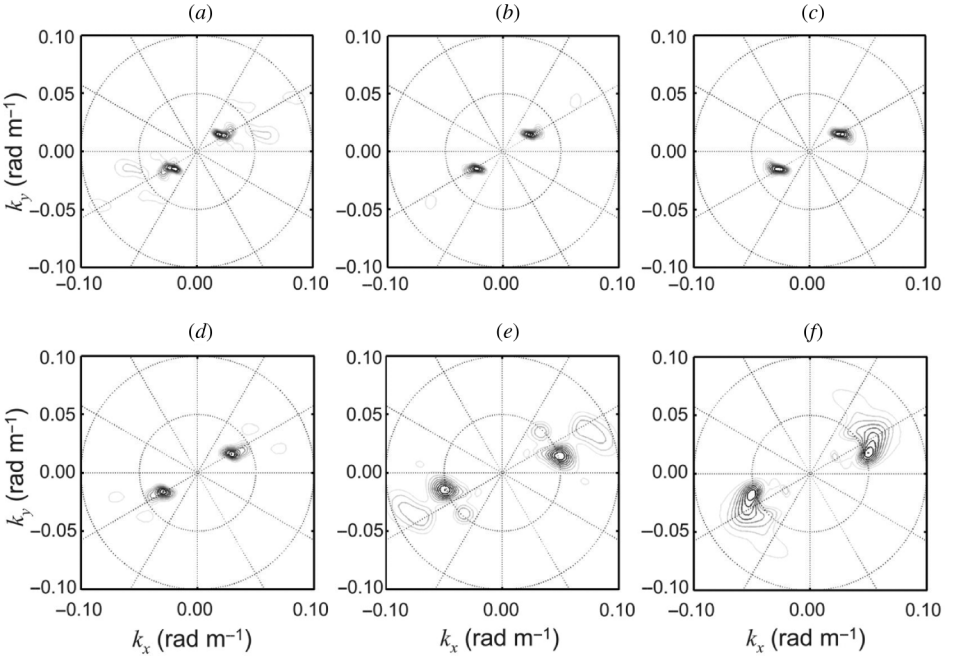

Figure 16. 2-D CWT image spectra analysed from the X-band radar image. Points A to F can be found in the image shown in figure 15.

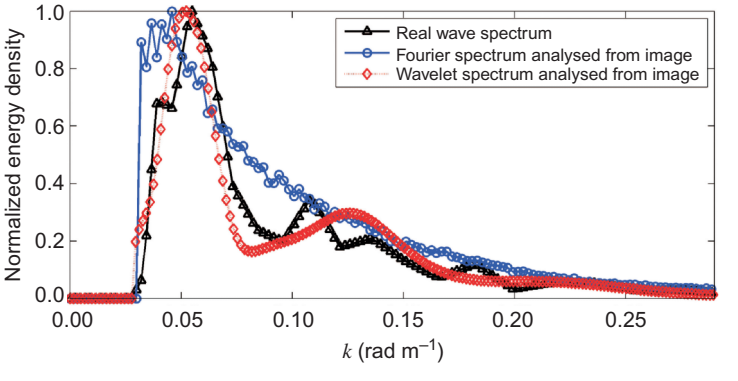

Figure 17. Comparison of the real wave spectrum, FFT spectrum and CWT spectrum.

the real wave spectra, the energy of image spectra is not direct ocean wave energy. To compare real wave spectra and image spectra, both the wave spectra and image spectra are normalized. The real wave spectrum provides local spectral features at the data buoy site. The Fourier spectrum presents spectral features of the whole radar image and energy from lower spatial frequencies ($k = 0.4$–0.5 rad m^{-1}) dominates the spectrum. The deviation between the peak spatial frequency of the real wave spectrum and the Fourier spectrum is obvious. Although the wavelet spectra are all calculated from the whole radar image, the local wavelet spectrum extracted from location C is similar to the real wave spectrum. Figure 15 shows that location C is quite close to the data

buoy location. This is why the CWT spectrum is similar to the real wave spectrum. Our work reveals that the image spectra using the 2-D CWT present local wave information clearly. The 2-D CWT should be an ideal method to present wave features from radar images.

By observing the wavelet spectra, this study noticed nonlinear features at the location from the shallower water image. Figure 18 shows the CWT spectra extracted at locations F and A of the radar image. The water depth at locations F and A are about 10 and 60 m, which belong to intermediate water and deep water, respectively, for most ocean wave cases within this area. To verify the relationship between energy and spatial frequency, we normalized both the energy and spatial frequency from all spectra. Some wavelet spectra in figure 18(*a*) show a second peak at around $2k_p$ where k_p, is the peak spatial frequency, which should be the effect of wave nonlinearity. By observing the wave spectra from ocean wave time series, Herbich (1990) pointed out that secondary spectral peak at a frequency that is about twice the main peak frequency is almost entirely composed of secondary nonlinear components that belong to the first group of bound waves. The nonlinearity of ocean waves is often conspicuous in coastal regions (Hara and Karachintsev 2003). The harmonic energy peak in the shallower water area is higher than that in the deeper water area. This means that the degree of nonlinearity in shallow water is higher than that in deeper water. Compared to figure 18(*a*), figure 18(*b*) presents the wavelet spectra extracted from location A of the same image. No obvious secondary spectral peak exists at $2k_p$, revealing the signal nonlinearity difference between images from intermediate water and deep water. By observing wave image nonlinearity, the wavelet spectra present local effects in different locations from the whole image.

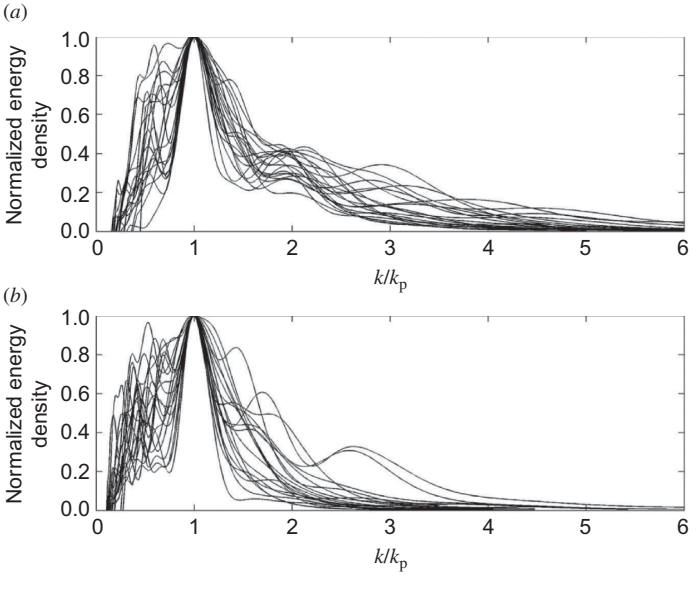

Figure 18. CWT spectra extracted from (*a*) intermediate water and (*b*) deep water.

5. Conclusions

Ocean remote sensing is a potential tool to present ocean wave information in the space domain. To extract wave information from images, applicable analysis algorithms are necessary. Owing to possible inhomogeneities within coastal wave field images, this study presents image spectra from remotely sensed images using a 2-D CWT.

The original theory of 2-D CWT has been proposed before; here, we present how to apply it to calculate local wave image spectra and optimize the algorithm. To speed up image analysis processing using the 2-D CWT algorithm, we simplify the wavelet function and apply the numerical technique of IFFT to reduce operation counts. Due to parameters from the wavelet function, such as $\boldsymbol{k}_0$ and ε, which influence image analysis using the 2-D CWT, this study has explored appropriate values for these parameters. Proper values of $\boldsymbol{k}_0$ and ε for applying the WT algorithm to image analysis have been proposed. The relationship between ocean wave conditions and the limit of image spatial resolution was also studied to understand the ideal conditions of an image. Because of the influence of window width, higher image spatial resolution is necessary for image analysis using 2-D CWT rather than by using 2-D FT.

Images observed from the satellite sensor and X-band radar are used here to verify the practicability of 2-D CWT. We present wave inhomogeneities from ocean remotely sensed images. The 2-D CWT image spectra reveal the phenomenon of wave refraction nearshore. The 2-D CWT spectra are capable of describing local wave information from different areas of an ocean image. Compared to real wave spectra from *in situ* measurements, the wavelet spectra show more accurate spatial frequency features to describe local wave features. The wavelet spectra also present wave nonlinearity from shallower water. By observing wave image nonlinearity, the wavelet spectra present local effects in different locations from the whole image. Different wave information obviously influences the design of coastal structures. For future applications of coastal areas, such as engineering design, disaster preparation and coastal management, local wave information must be extracted accurately. To describe local wave features in the space domain, 2-D CWT is an ideal tool.

Acknowledgements

This work was supported by the National Science Council (NSC98-2218-E-006-236 and NSC 98-2221-E-006-251) and the Water Resources Agency in Taiwan. The source for the satellite image dataset is the Global Land Cover Facility. The authors thank these agencies. In addition, the authors are grateful to the referees for helpful comments and suggestions.

References

Alpers, W. and Hasselmann, K., 1978, The two-frequency microwave technique for measuring ocean-wave spectra from an airplane or satellite. *Boundary-Layer Meteorology*, **13**, pp. 215–230.

Antoine, J.-P., Murenzi, R., Vandergheynst, P. and Twareque Ali, S., 2004, *Two-Dimensional Wavelets and their Relatives* (Cambridge: Cambridge University Press).

Carlson, G.E., 1995, Wavelet processing of SAR ocean wave images. In *Proceedings of International Geoscience and Remote Sensing Symposium, IGARSS '95*, 10–14 July 1995, Firenze, Italy, vol. 1, pp. 679–681.

Chen, C.C. and Chen, C.C., 1994, Gabor transform in texture analysis. In *Proceedings of SPIE – The International Society for Optical Engineering*, 31 October–2 November 1994, Bellingham, WA, USA, pp. 237–245.

Chuang, L.Z.H., Wu, L.C., Doong, D.J. and Kao, C.C., 2008, Two-dimensional continuous wavelet transform of simulated spatial images of waves on a slowly varying topography. *Ocean Engineering*, **35**, pp. 1039–1051.

Cracknell, A.P. and Varotsos, C.A., 2007, The IPCC fourth assessment report and the fiftieth anniversary of Sputnik. *Environmental Science and Pollution Research*, **14**, pp. 384–387.

Gangeskar, R., 2002, Ocean current estimated from X-band radar sea surface images. *IEEE Transactions on Geoscience and Remote Sensing*, **40**, pp. 783–792.

Gorman, R.M. and Hicks, D.M., 2005, Directional wavelet analysis of inhomogeneity in the surface wave field from aerial laser scanning data. *Journal of Physical Oceanography*, **35**, pp. 949–963.

Hara, T. and Karachintsev, A.V., 2003, Observation of nonlinear effects in ocean surface wave frequency spectra. *Journal of Physical Oceanography*, **33**, pp. 422–430.

Henderson, F.M. and Lewis, A.J., 1998, *Principles and Applications of Imaging Radar* (New York: John Wiley & Sons).

Herbich, J.B., 1990, *Handbook of Coastal and Ocean Engineering* (Houston, TX: Gulf Publishing Company).

Jahne, B., 1995, *Digital Image Processing: Concepts, Algorithms, and Scientific Applications* (Englewood Cliffs, NJ: Springer Verlag).

Jordan, D., Miksada, R.W. and Powers, E.J., 1997, Implementation of the continuous wavelet transform for digital time series analysis. *Reviews in Science Instruments*, **68**, pp. 1484–1494.

Kinsman, B., 1965, *Wind Waves, Their Generation and Propagation on the Ocean Surface* (Upper Saddle River, NJ: Prentice-Hall).

Lee, B.C., Wu, L.C., Doong, D.J. and Kao, C.C., 2007, Seasonal variations of wind and waves over Taiwan waters. *Marine Geophysical Researches*, **28**, pp. 183–190.

Nieto Borge, J.C., Rodriguez, G.R., Hessner, K. and Gonzalez, P.I., 2004, Inversion of marine radar images for surface wave analysis. *Journal of Atmospheric and Oceanic Technology*, **21**, pp. 1291–1300.

Priestley, M.B., 1991, *Non-Linear and Non-Stationary Time Series Analysis* (London: Academic Press Limited).

Tayfun, M.A., 1984, Random waves in water of variable depth. *Wave Motion*, **6**, pp. 119–125.

Van Name, F.W., 1960, *Modern Physics* (Upper Saddle River, NJ: Prentice-Hall).

Varotsos, C., Assimakopoulos, M.-N., and Efstathiou, M., 2007, Technical note: long-term memory effect in the atmospheric CO2 concentration at Mauna Loa. *Atmospheric Chemistry and Physics*, **7**, pp. 629–634.

Varotsos, C. and Kirk-Davidoff, D., 2006, Long-memory processes in ozone and temperature variations at the region 60° S–60° N. *Atmospheric Chemistry and Physics*, **6**, pp. 4093–4100.

Varotsos, C.A., Ondov, J.M., Cracknell, A.P., Efstathiou, M.N. and Assimakopoulos, M.N., 2006, Long-range persistence in global aerosol index dynamics. *International Journal of Remote Sensing*, **27**, pp. 3593–3603.

Young, I.R., 1999, *Wind Generated Ocean Waves* (Oxford: Elsevier Science Ltd).

Young, I.R., Rosenthal, W. and Ziemer, F., 1985, A three-dimensional analysis of marine radar images for the determination of ocean wave directionality and surface currents. *Journal of Geophysical Research*, **90**, pp. 1049–1059.